
Probabilistic Variational Contrastive Learning

Anonymous Author(s)

Affiliation
Address
email

Abstract

1 Deterministic embeddings learned by contrastive learning (CL) methods such as
2 SimCLR and SupCon achieve state-of-the-art performance but lack a principled
3 mechanism for uncertainty quantification. We propose *Variational Contrastive*
4 *Learning* (VCL), a decoder-free framework that maximizes the evidence lower
5 bound (ELBO) by interpreting the InfoNCE loss as a surrogate reconstruction
6 term and adding a KL divergence regularizer to a uniform prior on the unit hy-
7 persphere. We model the approximate posterior $q_\theta(z|x)$ as a projected normal
8 distribution, enabling the sampling of probabilistic embeddings. Our two instantia-
9 tions—VSimCLR and VSupCon—replace deterministic embeddings with samples
10 from $q_\theta(z|x)$ and incorporate a normalized KL term into the loss. Experiments
11 on multiple benchmarks demonstrate that VCL mitigates dimensional collapse,
12 enhances mutual information with class labels, and matches or outperforms deter-
13 ministic baselines in classification accuracy, all the while providing meaningful
14 uncertainty estimates through the posterior model. VCL thus equips contrastive
15 learning with a probabilistic foundation, serving as a new basis for contrastive
16 approaches.

17

1 Introduction

18 Deep representation learning seeks to map each input x into a compact embedding z that preserves
19 semantic similarity and facilitates downstream tasks such as classification or retrieval [5]. Contrastive
20 learning methods, including SimCLR [8] and SupCon [30], have advanced the state of the art by
21 pulling together positive pairs and pushing apart negatives in the embedding space. However, these
22 approaches rely on deterministic point estimates for each sample, which do not express uncertainty
23 or capture multiple plausible representations.

24 To address this limitation, we introduce a probabilistic *Variational Contrastive Learning* (VCL)
25 approach, which extends deterministic embeddings to *probabilistic embeddings* by maximizing
26 the evidence lower bound (ELBO) within the contrastive learning framework. Unlike variational
27 autoencoders (VAEs) [31], which employ a decoder to reconstruct inputs from latent variables, VCL
28 omits explicit decoders. Instead, we show that the InfoNCE loss can serve as a surrogate for the
29 ELBO reconstruction term, yielding a principled probabilistic formulation of contrastive learning.
30 Our VCL framework offers several new perspectives on learned embeddings.

31 Variational Contrastive Learning framework thus provides uncertainty-aware embeddings, a new
32 basis of CL with theoretical insights via the ELBO. Our contributions are summarized as follows:

33 • We introduce *Variational Contrastive Learning* (VCL), a decoder-free ELBO maximiza-
34 tion framework that reinterprets the InfoNCE loss as a surrogate reconstruction term and
35 incorporates a KL divergence regularizer to a uniform prior on the unit hypersphere.
36 • We propose a probabilistic embedding model using a projected normal posterior that enables
37 sampling, uncertainty quantification, and efficient KL computation on the hypersphere.

38 • We derive a connection between the optimal InfoNCE critic and the ELBO, showing that
 39 minimizing InfoNCE asymptotically maximizes the ELBO reconstruction term.
 40 • We demonstrate that VCL mitigates both dimensional collapse in self-supervised contrastive
 41 learning via the KL regularizer, while preserving embedding structure. We show that VCL
 42 methods preserve or improve mutual information with labels, match or exceed classification
 43 accuracy of deterministic baselines, and provide meaningful implication of distributional
 44 embeddings.

45 **2 Preliminaries**

46 Let $\mathcal{D} = \{(\mathbf{x}_i, \mathbf{y}_i)\}_{i=1}^N$ be a dataset of input $\mathbf{x} \in \mathcal{X}$ and label pairs drawn i.i.d. from the joint
 47 distribution $p(\mathbf{x}, \mathbf{y})$. An *encoder* $f_\theta: \mathcal{X} \rightarrow \mathbb{R}^d$, parameterized by θ , maps each input \mathbf{x} to a d -
 48 dimensional vector, which we then normalize to unit length: $\mathbf{z} = \frac{f_\theta(\mathbf{x})}{\|f_\theta(\mathbf{x})\|_2}$. Throughout this section,
 49 we define the temperature-scaled cosine similarity between embeddings \mathbf{z}_i and \mathbf{z}_j as

$$s(\mathbf{z}_i, \mathbf{z}_j) = \frac{\mathbf{z}_i^\top \mathbf{z}_j}{\tau}, \quad (1)$$

50 where $\tau > 0$ is the temperature hyperparameter. For any two probability distributions q and p , we
 51 denote the Kullback–Leibler (KL) divergence by $D(q \parallel p) = \mathbb{E}_{\mathbf{z} \sim q} \left[\log \frac{q(\mathbf{z})}{p(\mathbf{z})} \right]$.

52 **2.1 Self-Supervised Contrastive Learning**

53 Self-supervised contrastive learning (SSCL) learns representations from *unlabeled* data by pulling
 54 together embeddings of semantically related views (positives) and pushing apart those of unrelated
 55 views (negatives). For an anchor \mathbf{x} , let \mathbf{x}'_i denote a positive view sampled from $p(\mathbf{x}'_i \mid \mathbf{x})$, and let
 56 $\{\mathbf{x}'_j\}_{j \neq i}$ be $N - 1$ negative views drawn i.i.d. from the marginal $p(\mathbf{x}')$. The InfoNCE loss [43] for
 57 anchor \mathbf{x} is then

$$I_{\text{NCE}}(\mathbf{x}; \mathbf{x}') = -\mathbb{E}_{\substack{\mathbf{x} \sim p(\mathbf{x}) \\ \mathbf{x}' \sim p(\mathbf{x}' \mid \mathbf{x}) \\ \{\mathbf{x}'_j\}_{j \neq i} \sim p(\mathbf{x}')}} \left[\log \frac{\exp(s(\mathbf{z}, \mathbf{z}'_i))}{\sum_{j=1}^N \exp(s(\mathbf{z}, \mathbf{z}'_j))} \right], \quad (2)$$

58 where $\mathbf{z} = f_\theta(\mathbf{x})/\|f_\theta(\mathbf{x})\|_2$ and $s(\cdot, \cdot)$ is the temperature-scaled cosine similarity.

59 In practice, following SimCLR [8], we generate positives by applying two random augmentations
 60 $t', t'' \sim \mathcal{T}$ to each sample \mathbf{x}_i , yielding $(\mathbf{x}'_i, \mathbf{x}''_i) = (t'(\mathbf{x}_i), t''(\mathbf{x}_i))$.¹ All other $2N - 2$ augmented
 61 samples in the mini-batch serve as negatives. Let \mathcal{B} be the set of all $2N$ embeddings in the batch;
 62 then InfoNCE can be computed as

$$I_{\text{NCE}} = -\frac{1}{2N} \sum_{\mathbf{z} \in \mathcal{B}} \log \frac{\exp(s(\mathbf{z}, \mathbf{z}_p))}{\sum_{\mathbf{z}_n \in \mathcal{B} \setminus \{\mathbf{z}\}} \exp(s(\mathbf{z}, \mathbf{z}_n))}, \quad (3)$$

63 where \mathbf{z}_p denotes the positive embedding corresponding to \mathbf{z} . Since InfoNCE lower-bounds the
 64 mutual information $I(\mathbf{x}; \mathbf{x}')$ via $I(\mathbf{x}; \mathbf{x}') \geq \log N - I_{\text{NCE}}(\mathbf{x}; \mathbf{x}')$, we can see that minimizing I_{NCE}
 65 encourages encoders to preserve the semantic information of \mathbf{x} [48].

66 **2.2 Variational Inference and the Evidence Lower Bound (ELBO)**

67 In variational inference [6, 31], we treat the data distribution $p(\mathbf{x})$ as the marginal of a joint distribution
 68 over observed data \mathbf{x} and latent variables \mathbf{z} , i.e., $p(\mathbf{x}) = \int p(\mathbf{x}|\mathbf{z}) p(\mathbf{z}) d\mathbf{z}$. The latent variable \mathbf{z}
 69 captures meaningful structure in \mathbf{x} , serving both as a hidden cause and as a compressed representation
 70 for downstream tasks. In representation learning, we interpret \mathbf{z} as the embedding of \mathbf{x} .

71 The log-evidence can be written with respect to any approximate posterior $q_\phi(\mathbf{z}|\mathbf{x})$ as

$$\log p(\mathbf{x}) = \log \mathbb{E}_{q_\phi(\mathbf{z}|\mathbf{x})} \left[\frac{p(\mathbf{x}, \mathbf{z})}{q_\phi(\mathbf{z}|\mathbf{x})} \right]. \quad (4)$$

¹Although we adopt the SimCLR augmentation scheme, our method applies to any contrastive framework.

72 Rather than optimizing (4) directly, variational methods maximize the *evidence lower bound* (ELBO)
 73 obtained as a result of applying Jensen’s inequality:

$$\log p(\mathbf{x}) \geq \mathbb{E}_{q_\phi(\mathbf{z}|\mathbf{x})}[\log p(\mathbf{x}|\mathbf{z})] - D(q_\phi(\mathbf{z}|\mathbf{x}) \parallel p(\mathbf{z})) = \mathcal{L}^{\text{ELBO}}(\phi), \quad (5)$$

74 where $p(\mathbf{z})$ is a fixed prior (commonly $\mathcal{N}(\mathbf{0}, I_d)$). The ELBO decomposes into a *reconstruction* term
 75 $\mathbb{E}_q[\log p(\mathbf{x}|\mathbf{z})]$ and a *regularizer* $D(q_\phi(\mathbf{z}|\mathbf{x}) \parallel p(\mathbf{z}))$. Maximizing $\mathcal{L}^{\text{ELBO}}$ thus balances (i) accurate
 76 reconstruction, (ii) posterior-to-prior regularization, and (iii) posterior accuracy. By

$$\log p(\mathbf{x}) = \mathcal{L}^{\text{ELBO}}(\phi) + D(q_\phi(\mathbf{z}|\mathbf{x}) \parallel p(\mathbf{z}|\mathbf{x})), \quad (6)$$

77 for fixed $\log p(\mathbf{x})$, maximizing the ELBO minimizes the KL divergence between the approximate
 78 and true posteriors [6].

79 The ELBO provides a tractable surrogate for marginal likelihood that can be optimized by standard
 80 gradient methods. It will serve as the theoretical backbone of our Variational Contrastive Learning
 81 framework, offering both a probabilistic interpretation and explicit control over latent uncertainty.

82 **Relation to contrastive objectives.** Although the ELBO stems from latent-variable modeling,
 83 its two components align naturally with contrastive objectives: the KL divergence term enforces
 84 *uniformity* in the embedding space, while the reconstruction term promotes *alignment* between
 85 embeddings and observations. In Section 3, we leverage this connection by adopting distributional
 86 embeddings in the contrastive framework and incorporating a KL-based regularizer on the posterior.

87 3 Variational Contrastive Learning (VCL)

88 Unlike existing variational contrastive learning methods—which primarily focus on generative models
 89 with explicit decoders [7, 59]—our approach performs *decoder-free* ELBO maximization, making
 90 VCL a truly contrastive learning framework.

91 3.1 Decoder-Free ELBO Maximization

92 Here we describe how to optimize two terms in ELBO (5) within a purely contrastive learning setup.

93 **Reconstruction term.** The reconstruction term $\mathbb{E}_{q_\theta(\mathbf{z}|\mathbf{x})}[\log p(\mathbf{x}|\mathbf{z})]$ requires the true conditional
 94 $p(\mathbf{x}|\mathbf{z})$, which is generally intractable. Instead, we approximate it via the embedding conditional

$$p(\mathbf{z}'|\mathbf{z}) = \frac{p(\mathbf{z}, \mathbf{z}')}{\int p(\mathbf{z}, \mathbf{z}') d\mathbf{z}'}, \quad (7)$$

95 where $\mathbf{z}' \sim q_\theta(\cdot | \mathbf{x})$ captures semantics of \mathbf{x} . Thus,

$$\begin{aligned} \mathbb{E}_{q_\theta(\mathbf{z}|\mathbf{x})}[\log p(\mathbf{x}|\mathbf{z})] &\approx \mathbb{E}_{q_\theta(\mathbf{z}|\mathbf{x})q_\theta(\mathbf{z}'|\mathbf{x})}[\log p(\mathbf{z}'|\mathbf{z})] \\ &= \mathbb{E}\left[\log \frac{p(\mathbf{z}, \mathbf{z}')}{\int p(\mathbf{z}, \mathbf{z}') d\mathbf{z}'}\right] \approx \mathbb{E}\left[\log \frac{e^{\psi(\mathbf{z}, \mathbf{z}')}}{\sum_j e^{\psi(\mathbf{z}, \mathbf{z}'_j)}}\right], \end{aligned} \quad (8)$$

96 where we approximate $p(\mathbf{z}, \mathbf{z}') \approx e^{\psi(\mathbf{z}, \mathbf{z}')}$ via a critic ψ . Details on parameterizing $p(\mathbf{z}' | \mathbf{z})$
 97 appear in Section 3.2. The following lemma supports the approximation $\mathbb{E}_{q_\theta(\mathbf{z}|\mathbf{x})}[\log p(\mathbf{x}|\mathbf{z})] \approx$
 98 $\mathbb{E}_{q_\theta(\mathbf{z}|\mathbf{x})q_\theta(\mathbf{z}'|\mathbf{x})}[\log p(\mathbf{z}'|\mathbf{z})]$. A further discussion on the approximation in (8) and a tightness
 99 condition is in Appendix D.1.

100 **Lemma 3.1.** *Let \mathbf{x} and \mathbf{z} be conditionally independent given \mathbf{z}' . Then, the reconstruction term in
 101 Section 3.1 is bounded as*

$$\mathbb{E}_{q(\mathbf{z}|\mathbf{x})}[\log p(\mathbf{x}|\mathbf{z})] \geq \mathbb{E}_{q(\mathbf{z}|\mathbf{x})q(\mathbf{z}'|\mathbf{x})}[\log p(\mathbf{z}'|\mathbf{z})] + \text{const.}, \quad (9)$$

102 where const. is independent of \mathbf{z} .

103 *Proof.* The proof of Proposition 3.1 is in Appendix B.1. \square

104 Noting that the right-hand side of (8) is (up to sign) the InfoNCE surrogate, setting $\psi(\cdot, \cdot) = s(\cdot, \cdot)$ in
 105 (8) where $s(\cdot, \cdot)$ is defined in (1) yields

$$\mathbb{E}_{q_\theta(\mathbf{z}|\mathbf{x})} [\log p(\mathbf{x}|\mathbf{z})] \approx -I_{\text{NCE}}(\mathbf{x}; \mathbf{x}'). \quad (10)$$

106 Hence, minimizing the InfoNCE loss maximizes the reconstruction term without explicit decoders.

107 In contrast to VAE embeddings—which often rely on pixel-level reconstruction through expressive
 108 decoder [53]—VCL preserves semantics via contrastive objectives. The next proposition (proved in
 109 Appendix B.2) provides a theoretical connection between InfoNCE and the reconstruction term.

110 **Proposition 3.2.** *Assume that: 1) the critic ψ in InfoNCE is optimal; 2) $p(\mathbf{z}) < \infty$, $\forall \mathbf{z}$; and 3)
 111 $0 < \epsilon \leq p(\mathbf{z}|\mathbf{z}') \leq g_+(\mathbf{z})$, $\forall \mathbf{z}, \mathbf{z}'$ with a absolutely integrable $g : \mathcal{Z} \rightarrow (0, \infty)$. Then, as the
 112 number of negatives $N \rightarrow \infty$,*

$$-I_{\text{NCE}}(\mathbf{x}; \mathbf{x}') + \log N \longrightarrow \mathbb{E} [\log p(\mathbf{z}'|\mathbf{z})] - D(q_\theta(\mathbf{z}'|\mathbf{x}) \| p(\mathbf{z}')) - H(q_\theta(\mathbf{z}'|\mathbf{x})), \quad (11)$$

113 where the expectation is over $q_\theta(\mathbf{z}|\mathbf{x})q_\theta(\mathbf{z}'|\mathbf{x})$, and $H(\cdot)$ denotes entropy.

114 **Regularization.** Maximizing the ELBO requires choosing a prior $p(\mathbf{z})$ and an approximate posterior
 115 $q_\theta(\mathbf{z} \mid \mathbf{x})$. Although both are often taken as Gaussian distributions [31], this choice conflicts
 116 with the geometry of contrastive embeddings, which often lie on the unit hypersphere due to the
 117 normalization [62]. Instead, we adopt non-Gaussian priors and posteriors—one key distinction from
 118 standard VAE approaches.

119 Motivated by the uniformity property [62] on the unit sphere $\mathcal{S}^{d-1} = \{\mathbf{z} \in \mathbb{R}^d : \|\mathbf{z}\|_2 = 1\}$, we
 120 set the prior $p(\mathbf{z})$ to be the uniform distribution over \mathcal{S}^{d-1} . For the approximate posterior, we use
 121 the *projected normal* distribution [22], which admits efficient KL-divergence computation while
 122 enforcing $\mathbf{z} \in \mathcal{S}^{d-1}$. A random variable $\mathbf{z} \sim \mathcal{PN}(\mu, K)$ is obtained by sampling

$$\mathbf{z} = \frac{\mathbf{u}}{\|\mathbf{u}\|_2} \quad \text{with} \quad \mathbf{u} \sim \mathcal{N}(\mu, K). \quad (12)$$

123 In particular, $\mathcal{PN}(0, I_d)$ reduces to the uniform distribution on \mathcal{S}^{d-1} , i.e., $\mathcal{PN}(0, I_d) \stackrel{d}{=} \text{Unif}(\mathcal{S}^{d-1})$.

124 With $q_\theta(\mathbf{z}|\mathbf{x}) = \mathcal{PN}(\mu, K)$, the regularization term becomes

$$D(q_\theta(\mathbf{z}|\mathbf{x}) \| p(\mathbf{z})) = D(\mathcal{PN}(\mu, K) \| \text{Unif}(\mathcal{S}^{d-1})). \quad (13)$$

125 Since a closed-form KL divergence between projected normals and the uniform sphere is intractable,
 126 we instead minimize the Gaussian KL as an upper bound—by the data processing inequality [47]:

$$D(\mathcal{N}(\mu, K) \| \mathcal{N}(0, I_d)) \geq D(\mathcal{PN}(\mu, K) \| \text{Unif}(\mathcal{S}^{d-1})). \quad (14)$$

127 In Appendix D.2, we analyze the tightness of the gap in (14) and show that the Gaussian KL
 128 divergence closely approximates the projected-normal KL divergence; the two exhibit nearly identical
 129 behavior throughout VCL training.

130 For $K = \text{diag}(\sigma_1^2, \dots, \sigma_d^2)$, the Gaussian KL admits the closed form

$$D(\mu, K) = \frac{1}{2} \sum_{i=1}^d (\sigma_i^2 + \mu_i^2 - 1 - \log \sigma_i^2). \quad (15)$$

131 The KL divergence term $D(\mu, K)$ grows linearly with the embedding dimension d , which can
 132 destabilize training when d is large. To address this, we normalize the KL term by d , i.e., $\tilde{D}(\mu, K) = \frac{1}{d} D(\mu, K)$, so that its magnitude remains comparable to the InfoNCE loss.

134 **Final objective for maximizing ELBO.** By combining (10) and (15), we obtain the following
 135 (approximate) lower bound on the ELBO:

$$\mathcal{L}^{\text{ELBO}}(\theta) \geq -I_{\text{NCE}}(\mathbf{x}; \mathbf{x}') - D(\mu_{\mathbf{x}}, K_{\mathbf{x}}), \quad (16)$$

136 where $\mu_{\mathbf{x}}$ and $K_{\mathbf{x}} = \text{diag}(\sigma_{\mathbf{x},1}, \dots, \sigma_{\mathbf{x},d})$ are the parameters of $q_\theta(\mathbf{z} \mid \mathbf{x})$. Because this bound is
 137 asymmetric in $(\mathbf{x}, \mathbf{x}')$, we symmetrize it to define our final VCL objective:

$$\mathcal{L}^{\text{VCL}} = \frac{1}{2} \left(I_{\text{NCE}}(\mathbf{x}; \mathbf{x}') + I_{\text{NCE}}(\mathbf{x}'; \mathbf{x}) + D(\mu_{\mathbf{x}}, K_{\mathbf{x}}) + D(\mu_{\mathbf{x}'}, K_{\mathbf{x}'}) \right). \quad (17)$$

138 Minimizing \mathcal{L}^{VCL} therefore maximizes the ELBO. Next, we introduce Variational SimCLR (VSim-
 139 CLR), which is specifically designed to optimize this objective efficiently.

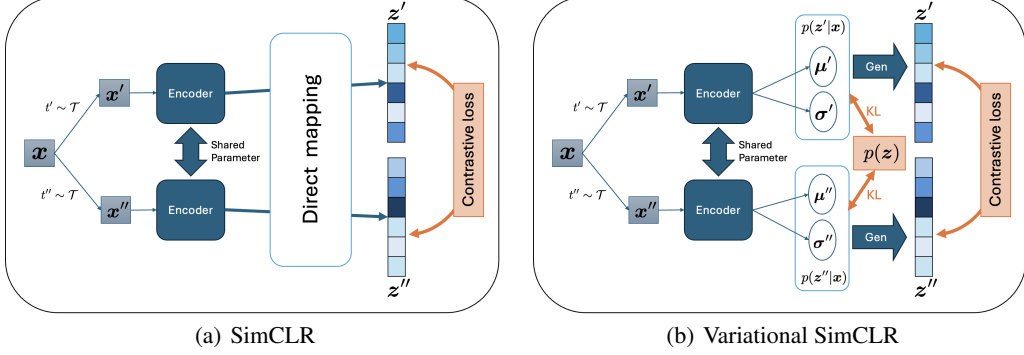


Figure 1: Graphical illustration of SimCLR and Variational SimCLR (VSimCLR).

140 3.2 Variational SimCLR (VSimCLR)

141 We propose *Variational SimCLR* (VSimCLR), whose architecture is illustrated in Figure 1(b). VSim-
142 CLR minimizes \mathcal{L}^{VCL} in (17), thereby implicitly maximizing the ELBO and bringing the approximate
143 posterior closer to the true posterior by (6). Compared to SimCLR, VSimCLR differs in three key
144 aspects: (i) the encoder outputs the parameters of a variational posterior rather than deterministic
145 embeddings; (ii) embeddings are sampled from this posterior; and (iii) a KL divergence term between
146 the approximate posterior and the prior is included in the loss.

147 Specifically, during training, each input \mathbf{x} is first augmented twice to obtain \mathbf{x}' and \mathbf{x}'' , as in SimCLR.
148 The encoder then maps \mathbf{x}' and \mathbf{x}'' to posterior parameters (μ', σ') and (μ'', σ'') , respectively. We
149 then sample

$$z' = \mu' + \text{diag}(\sigma') \epsilon_1, \quad \text{and} \quad z'' = \mu'' + \text{diag}(\sigma'') \epsilon_2, \quad (18)$$

150 where $\epsilon_1, \epsilon_2 \stackrel{\text{i.i.d.}}{\sim} \mathcal{N}(\mathbf{0}, I_d)$. After normalizing \mathbf{z}' and \mathbf{z}'' to unit length, we compute the InfoNCE loss
151 over the normalized embeddings in the batch and add the KL divergence

$$\frac{1}{d} D(\mathcal{N}(\mu, \text{diag}(\sigma^2)) \parallel \mathcal{N}(\mathbf{0}, I_d)) \quad (19)$$

152 for each sample. Minimizing this combined objective effectively minimizes \mathcal{L}^{VCL} in (17) and thus
153 maximizes the ELBO. Figure 1 highlights these differences: VSimCLR replaces deterministic em-
154 beddings with the projected-normal posterior $\mathcal{PN}(\mu, \text{diag}(\sigma^2))$ and regularizes it via KL divergence
155 to the standard normal.²

156 4 Experiments

157 We evaluate VCL with SimCLR and SupCon across five aspects: (i) embedding visualization, (ii)
158 dimensional collapse, (iii) mutual information between embeddings and labels, (iv) classification
159 accuracy, and (v) implications of distributional embeddings. Implementation and training details are
160 provided in Appendix E.1.

161 4.1 Embedding Visualization

162 Figure 2 presents t-SNE [57] and UMAP [40] projections of the embeddings learned by SimCLR and
163 VSimCLR on the CIFAR-10 test set. Although VSimCLR incorporates an additional KL-regularizer,
164 it preserves the characteristic cluster structure induced by contrastive learning. This confirms that our
165 distributional embeddings retain the semantic information learned by contrastive methods.

166 4.2 Dimensional Collapse

²An analogy with SupCon, namely VSupCon, is provided in Appendix C.

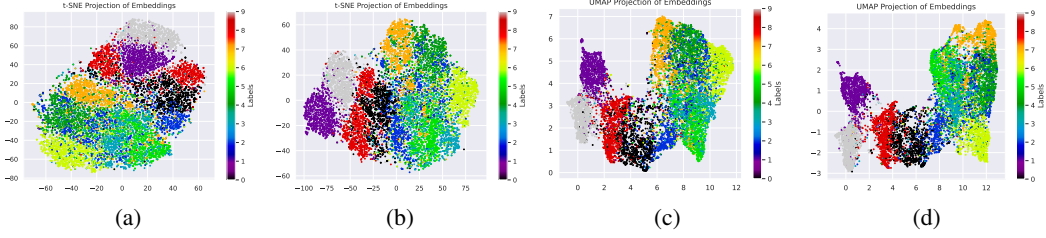


Figure 2: Embedding visualization for SimCLR and VSimCLR on CIFAR-10 test set. (a) t-SNE of SimCLR; (b) t-SNE of VSimCLR; (c) UMAP of SimCLR; (d) UMAP of VSimCLR. VSimCLR preserves the characteristic cluster structure of contrastive learning while introducing probabilistic embeddings regularized by (15).

Table 1: Classification accuracy on various datasets. We report top-1 and top-5 accuracies of SimCLR, VSimCLR, SupCon, and VSupCon across the datasets.

METHOD	CIFAR-10		CIFAR-100		TINY-IMAGENET		STL10		CALTECH256	
	TOP1	TOP5	TOP1	TOP5	TOP1	TOP5	TOP1	TOP5	TOP1	TOP5
SIMCLR	78.42	98.52	49.56	78.84	38.95	66.89	60.44	95.80	43.14	66.15
VSimCLR	81.48	98.95	54.58	82.87	37.70	66.06	60.11	92.00	48.50	69.99
SupCon	93.60	99.71	70.79	89.11	57.60	77.16	75.88	98.51	87.06	91.64
VSupCon	93.85	99.68	71.66	89.42	48.30	72.84	75.76	96.99	83.06	91.29

167 Contrastive learning methods such as SimCLR often suffer from
168 *dimensional collapse*, where embeddings concentrate in a low-
169 dimensional subspace, underutilizing the full capacity of the
170 representation space [29]. To quantify this effect, let $\{\mathbf{z}_i\}_{i=1}^N$
171 be the test-set embeddings and their covariance matrix $C =$
172 $\frac{1}{N} \sum_{i=1}^N (\mathbf{z}_i - \bar{\mathbf{z}})(\mathbf{z}_i - \bar{\mathbf{z}})^\top$, with $\bar{\mathbf{z}} = \frac{1}{N} \sum_{i=1}^N \mathbf{z}_i$. Figure 3
173 shows the singular values of C for SimCLR and VSimCLR.
174 VSimCLR produces a substantially flatter spectrum, indicating
175 a higher effective rank and thus mitigating dimensional collapse.
176 Remarkably, on CIFAR-100, VSimCLR nearly doubles the
177 number of dominant components compared to SimCLR. These
178 results demonstrate that VSimCLR not only preserves semantic
179 clustering but also leverages the embedding space more fully, and can be combined with other
180 collapse-mitigation strategies for further gains. Additional experiments on Caltech-256 and Tiny-
181 ImageNet (Figure 8, Appendix E.2) exhibit similar behavior.

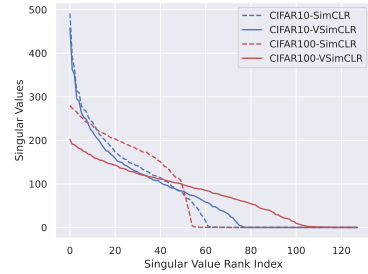


Figure 3: Singular-value spectrum.

182 4.3 Mutual Information Comparison

183 Figure 4 reports the estimated mutual information $I(\mathbf{z}; \mathbf{c})$ between
184 the learned embeddings \mathbf{z} and their true class labels \mathbf{c} of CIFAR-10.
185 We compute this using the Mixed KSG estimator [13], which is
186 well-suited for mixed or multimodal distributions.

187 Both VSimCLR and VSupCon achieve mutual information on par
188 with—or slightly exceeding—their non-variational counterparts. In
189 particular, during the first 200 epochs, VSimCLR exhibits lower
190 mutual information than SimCLR, reflecting the added optimization
191 challenge of the KL regularizer. After this initial phase, VSimCLR
192 surpasses SimCLR and maintains higher mutual information for
193 the remainder of training. These results indicate that VSimCLR
194 ultimately preserves—or even improves—information between em-
195 beddings and labels, while also producing rich distributional representations.

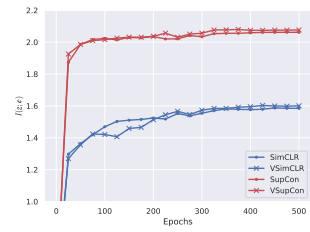


Figure 4: Estimate of $I(\mathbf{z}; \mathbf{c})$.

196 **4.4 Classification**

197 For classification, we use the posterior mean μ_x as the embedding and train a linear classifier.
 198 Table 1 reports Top-1 and Top-5 accuracies on CIFAR-10, CIFAR-100, Tiny-ImageNet, STL-10,
 199 and Caltech-256. VSimCLR outperforms SimCLR on CIFAR-10 ($78.42 \rightarrow 81.48$) and CIFAR-
 200 100 ($49.56 \rightarrow 54.58$) in Top-1 accuracy, with similar gains in Top-5. On Caltech-256, VSimCLR
 201 also improves Top-1 accuracy substantially. Performance on Tiny-ImageNet and STL-10 remains
 202 comparable, with slight decreases (within experimental variance) likely due to the KL regularizer.
 203 SupCon provides supervised baselines, and VSupCon further improves Top-1 accuracy on CIFAR-10
 204 ($93.60 \rightarrow 93.85$) and CIFAR-100 ($70.79 \rightarrow 71.66$). Modest declines on Tiny-ImageNet, STL-10,
 205 and Caltech-256 reflect the trade-off of adding the KL term on datasets with higher complexity or
 206 fewer samples.
 207 Although VCL is not explicitly designed to boost classification accuracy, VSimCLR consistently
 208 match or exceed their deterministic counterparts. This demonstrates that distributional embeddings
 209 preserve the alignment and uniformity properties [62], while providing meaningful uncertainty proxy.

210 **4.5 Implications of Distributional Embeddings**

211 We illustrate the interpretability of distributional embeddings using examples from CIFAR-10. Figure 9 displays sample images
 212 alongside the log-determinant $\log \det(K)$ of their posterior covariance K learned by VSimCLR. Top-row images are common
 213 class members and exhibit larger $\log \det(K)$ —indicating broader
 214 posterior dispersion—whereas bottom-row images are atypical or
 215 uncommon with smaller $\log \det(K)$, reflecting more concentrated
 216 posteriors.³

217 We quantify the relationship between posterior covariance and
 218 uncertainty using CIFAR-10H [46] and CIFAR-10C [19]. Figure 5 plots $\log \det(K)$ against the entropy of the CIFAR-10H soft
 219 labels [24, 25]; the negative slope of the linear fit (red line) indicates that images with lower $\log \det(K)$ —i.e., more concentrated
 220 posteriors—tend to have higher label entropy and thus greater
 221 ambiguity. Next, using CIFAR-10C, we examine how posterior
 222 covariance varies with corruption severity, which correlates with
 223 label uncertainty. Figures 6 and 11 show that $\log \det(K)$ decreases
 224 as corruption strength increases, implying that lower posterior dispersion corresponds to higher
 225 uncertainty, consistent with Figure 5.
 226

227 These results demonstrate that the dispersion of the learned posterior correlates with semantic
 228 uncertainty, highlighting the practical interpretability of VCL’s distributional embeddings. As an
 229 example application of posterior covariance, we consider CIFAR-100 under a label-scarce setting in
 230 which only a small number of labels per class are available to train a linear classifier. Table 2 reports
 231 accuracies for SimCLR, VSimCLR, and VSimCLR+wt, with classifiers trained using cross-entropy
 232 (CE). Here, “+wt” denotes a weighted CE in which sample weights are proportional to posterior
 233 covariance to downweight ambiguous examples. Specifically, we use

$$\mathcal{L}_{wCE} = \sum_{i=1}^N w_i \log \phi_{c_i}(\mathbf{z}_i), \text{ with } w_i \propto \log \det(K) \text{ (after normalization),} \quad (20)$$

234 where $\phi_{c_i}(\mathbf{z}_i)$ is the estimated probability of the true class. Table 2 shows that VCL variants improve
 235 over SimCLR and SupCon, with smaller gains for SupCon since it already leverages labels during
 236 pretraining. Moreover, weighting by posterior covariance further improves performance, supporting

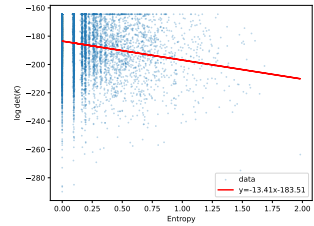


Figure 5: Posterior dispersion versus label ambiguity. Each point plots $\log \det(K)$ against the entropy of human-annotated class probabilities from CIFAR-10H, with a first-order linear fit (red line).

³ $\log \det K$ quantifies the *dispersion of the posterior in embedding space*, which reflects *typicality* rather than label uncertainty. Larger values correspond to more “typical” samples with many latent realizations consistent with the data manifold, whereas smaller values indicate more “unique” or outlier samples with tightly concentrated posteriors. A generative analogy may help understanding: if an outlier image had an extremely large posterior variance, then samples drawn from the prior would reproduce that outlier far too often—contradicting its rarity. Hence, larger variance corresponds to “typical” not “uncertain” inputs.

Table 2: Classification accuracy on CIFAR-100 with label scarcity. We use ResNet-18 back-bone and same augmentations for all experiments. We sample the labelled subset once and report the mean accuracy of five runs with (standard error).

METHODS	1 LABELS / CLASS	3 LABELS / CLASS	5 LABELS / CLASS	10 LABELS / CLASS	20 LABELS / CLASS
SIMCLR	12.22 (0.12)	21.37 (0.15)	26.37 (0.01)	33.09 (0.11)	38.00 (0.06)
VSimCLR	15.57 (0.09)	25.70 (0.19)	30.89 (0.11)	37.40 (0.08)	42.13 (0.10)
VSimCLR+WT	15.97 (0.08)	26.07 (0.20)	31.12 (0.06)	37.48 (0.08)	42.36 (0.03)
SUPCON	71.55 (0.04)	71.56 (0.05)	71.64 (0.02)	71.65 (0.03)	72.07 (0.05)
VSUPCON	71.77 (0.12)	71.79 (0.10)	71.96 (0.09)	72.07 (0.05)	72.16 (0.04)
VSUPCON+WT	71.87 (0.02)	71.78 (0.07)	71.94 (0.07)	72.07 (0.07)	72.16 (0.06)

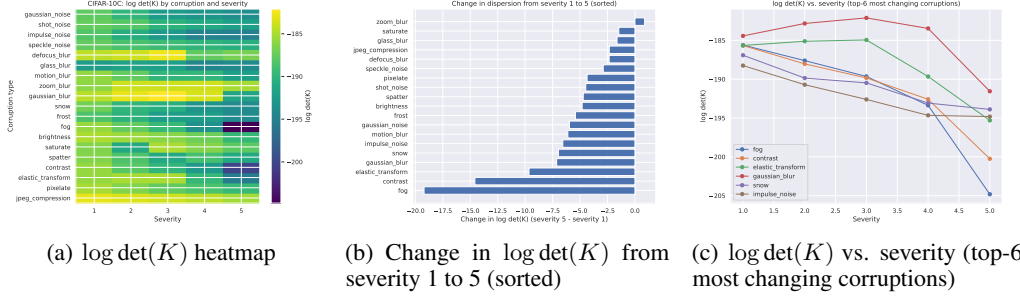


Figure 6: $\log \det(K)$ of **VSimCLR** embeddings on CIFAR-10C under different corruption types and severities. “Severity” denotes the corruption level. The observed negative correlation between $\log \det(K)$ and severity is consistent with our finding that more uncertain samples exhibit smaller posterior covariance dispersion. Exact $\log \det(K)$ values are in Table 7.

240 distributional embeddings as a confidence proxy. Additional experiments and discussion on posterior
241 distributions and label uncertainty are provided in Appendix E.5.

242 This counterintuitive finding—that typical (i.e., common) samples exhibit larger posterior dispersion—
243 parallels the observation in concurrent work by Guth et al. [16], albeit under different settings:
244 (i) Quantity: we analyze latent-space posterior covariance via $\log \det K$, whereas they study input-
245 space marginal density $p(x)$; (ii) Observation: typical samples have larger $\log \det K$, while they
246 have lower marginal density. Although the quantities are measured in different spaces, both results
247 indicate that typical samples are not the highest-density points. In our case, typical images yield larger
248 posterior dispersion and atypical images smaller dispersion; since dispersion is inversely related to
249 peak density, our result aligns with Guth et al.’s observation. Hence, in both settings, “typical” \neq
250 “highest-density.”

251 5 Conclusion

252 We have introduced *Variational Contrastive Learning* (VCL), a decoder-free ELBO-maximization
253 framework that endows contrastive learning with principled probabilistic embeddings. By interpreting
254 InfoNCE as a surrogate reconstruction term and regularizing with a KL divergence to a uniform prior
255 on the unit sphere, VCL enables distributional encodings without explicit decoders. We instantiated
256 VCL in two variants—VSimCLR and VSUPCon—by replacing deterministic embeddings with
257 samples from $q_\theta(z | x)$ and adding a normalized KL term.

258 Theoretical and empirical results show that VCL preserves the properties of contrastive embeddings,
259 mitigates dimensional collapse, maintains or improves mutual information with labels, and matches or
260 exceeds deterministic baselines in classification accuracy, while also providing meaningful posterior
261 uncertainty estimates. We further analyzed the implications of probabilistic embeddings—spanning
262 label uncertainty, typicality, and OOD behavior—through posterior-covariance dispersion. We also
263 observed a counterintuitive but consistent pattern, echoed in concurrent diffusion-model work [16]:
264 lower posterior-covariance dispersion is associated with higher sample uniqueness (i.e., more atypical
265 or outlier examples), whereas typical samples exhibit larger posterior covariance dispersion.

266 **References**

267 [1] L. Aitchison and S. Ganev. Infonce is variational inference in a recognition parameterised
268 model. *arXiv preprint arXiv:2107.02495*, 2021.

269 [2] C. A. Barbano, B. Dufumier, E. Tartaglione, M. Grangetto, and P. Gori. Unbiased supervised
270 contrastive learning. *arXiv preprint arXiv:2211.05568*, 2022.

271 [3] A. Bardes, J. Ponce, and Y. LeCun. Vicreg: Variance-invariance-covariance regularization for
272 self-supervised learning. *arXiv preprint arXiv:2105.04906*, 2021.

273 [4] P. L. Bartlett, D. J. Foster, and M. J. Telgarsky. Spectrally-normalized margin bounds for neural
274 networks. *Advances in neural information processing systems*, 30, 2017.

275 [5] Y. Bengio, A. Courville, and P. Vincent. Representation learning: A review and new perspectives.
276 *IEEE transactions on pattern analysis and machine intelligence*, 35(8):1798–1828, 2013.

277 [6] D. M. Blei, A. Kucukelbir, and J. D. McAuliffe. Variational inference: A review for statisticians.
278 *Journal of the American statistical Association*, 112(518):859–877, 2017.

279 [7] L. Chen, P. Wang, X. Han, and L. Xu. Multi-relational variational contrastive learning for next
280 poi recommendation. In *ICASSP 2025 - 2025 IEEE International Conference on Acoustics,
281 Speech and Signal Processing (ICASSP)*, pages 1–5, 2025.

282 [8] T. Chen, S. Kornblith, M. Norouzi, and G. Hinton. A simple framework for contrastive learning
283 of visual representations. In *International conference on machine learning*, pages 1597–1607.
284 PMLR, 2020.

285 [9] S. Chopra, R. Hadsell, and Y. LeCun. Learning a similarity metric discriminatively, with
286 application to face verification. In *2005 IEEE computer society conference on computer vision
287 and pattern recognition (CVPR'05)*, volume 1, pages 539–546. IEEE, 2005.

288 [10] C.-Y. Chuang, J. Robinson, Y.-C. Lin, A. Torralba, and S. Jegelka. Debiased contrastive learning.
289 *Advances in neural information processing systems*, 33:8765–8775, 2020.

290 [11] A. Coates, A. Ng, and H. Lee. An analysis of single-layer networks in unsupervised feature
291 learning. In *Proceedings of the fourteenth international conference on artificial intelligence
292 and statistics*, pages 215–223. JMLR Workshop and Conference Proceedings, 2011.

293 [12] A. Ermolov, A. Siarohin, E. Sangineto, and N. Sebe. Whitening for self-supervised represen-
294 tation learning. In *International conference on machine learning*, pages 3015–3024. PMLR,
295 2021.

296 [13] W. Gao, S. Kannan, S. Oh, and P. Viswanath. Estimating mutual information for discrete-
297 continuous mixtures. *Advances in neural information processing systems*, 30, 2017.

298 [14] R. Girdhar, A. El-Nouby, Z. Liu, M. Singh, K. V. Alwala, A. Joulin, and I. Misra. Imagebind:
299 One embedding space to bind them all. In *Proceedings of the IEEE/CVF Conference on
300 Computer Vision and Pattern Recognition*, pages 15180–15190, 2023.

301 [15] G. Griffin, A. Holub, P. Perona, et al. Caltech-256 object category dataset. Technical report,
302 Technical Report 7694, California Institute of Technology Pasadena, 2007.

303 [16] F. Guth, Z. Kadkhodaie, and E. P. Simoncelli. Learning normalized image densities via dual
304 score matching. *arXiv preprint arXiv:2506.05310*, 2025.

305 [17] J. He, J. Du, and W. Ma. Preventing dimensional collapse in self-supervised learning via
306 orthogonality regularization. *arXiv preprint arXiv:2411.00392*, 2024.

307 [18] K. He, X. Zhang, S. Ren, and J. Sun. Deep residual learning for image recognition. In
308 *Proceedings of the IEEE conference on computer vision and pattern recognition*, pages 770–
309 778, 2016.

310 [19] D. Hendrycks and T. Dietterich. Benchmarking neural network robustness to common corrup-
311 tions and perturbations. *Proceedings of the International Conference on Learning Representa-
312 tions*, 2019.

313 [20] D. Hendrycks, N. Mu, E. D. Cubuk, B. Zoph, J. Gilmer, and B. Lakshminarayanan. Augmix: A
 314 simple data processing method to improve robustness and uncertainty. In *Proc. International*
 315 *Conference on Learning Representations (ICLR)*, 2020.

316 [21] A. Hermans, L. Beyer, and B. Leibe. In defense of the triplet loss for person re-identification.
 317 *arXiv preprint arXiv:1703.07737*, 2017.

318 [22] D. Hernandez-Stumpfhauser, F. J. Breidt, and M. J. van der Woerd. The general projected
 319 normal distribution of arbitrary dimension: Modeling and bayesian inference. 2017.

320 [23] N. M. Hieu, A. Ledent, Y. Lei, and C. Y. Ku. Generalization analysis for deep contrastive
 321 representation learning. In *Proceedings of the AAAI Conference on Artificial Intelligence*,
 322 volume 39, pages 17186–17194, 2025.

323 [24] T. Ishida, I. Yamane, N. Charoenphakdee, G. Niu, and M. Sugiyama. Is the performance of
 324 my deep network too good to be true? a direct approach to estimating the bayes error in binary
 325 classification. In *The Eleventh International Conference on Learning Representations*, 2023.

326 [25] M. Jeong, M. Cardone, and A. Dytso. Demystifying the optimal performance of multi-class
 327 classification. In A. Oh, T. Naumann, A. Globerson, K. Saenko, M. Hardt, and S. Levine,
 328 editors, *Advances in Neural Information Processing Systems*, volume 36, pages 31638–31664.
 329 Curran Associates, Inc., 2023.

330 [26] M. Jeong, M. Cardone, and A. Dytso. Data-driven estimation of the false positive rate of the
 331 bayes binary classifier via soft labels. In *2024 IEEE International Symposium on Information*
 332 *Theory (ISIT)*, pages 368–373, 2024.

333 [27] M. Jeong and A. Hero. Generalizing supervised contrastive learning: A projection perspective.
 334 *arXiv preprint arXiv:2506.09810*, 2025.

335 [28] M. Jeong, M. Namgung, Z. M. Kim, D. Kang, Y.-Y. Chiang, and A. Hero. Anchors aweigh!
 336 sail for optimal unified multi-modal representations. *arXiv preprint arXiv:2410.02086*, 2024.

337 [29] L. Jing, P. Vincent, Y. LeCun, and Y. Tian. Understanding dimensional collapse in contrastive
 338 self-supervised learning. *arXiv preprint arXiv:2110.09348*, 2021.

339 [30] P. Khosla, P. Teterwak, C. Wang, A. Sarna, Y. Tian, P. Isola, A. Maschinot, C. Liu, and
 340 D. Krishnan. Supervised contrastive learning. *Advances in neural information processing*
 341 *systems*, 33:18661–18673, 2020.

342 [31] D. P. Kingma, M. Welling, et al. An introduction to variational autoencoders. *Foundations and*
 343 *Trends® in Machine Learning*, 12(4):307–392, 2019.

344 [32] M. Kirchhof, E. Kasneci, and S. J. Oh. Probabilistic contrastive learning recovers the correct
 345 aleatoric uncertainty of ambiguous inputs. In *International Conference on Machine Learning*,
 346 pages 17085–17104. PMLR, 2023.

347 [33] A. Krizhevsky, G. Hinton, et al. Learning multiple layers of features from tiny images. 2009.

348 [34] A. Krizhevsky, I. Sutskever, and G. E. Hinton. Imagenet classification with deep convolutional
 349 neural networks. In *Proc. Advances in Neural Information Processing Systems (NeurIPS)*,
 350 volume 25, pages 1097–1105, 2012.

351 [35] Y. Le and X. Yang. Tiny imagenet visual recognition challenge. *CS 231N*, 7(7):3, 2015.

352 [36] Y. Lei, T. Yang, Y. Ying, and D.-X. Zhou. Generalization analysis for contrastive representation
 353 learning. In *International Conference on Machine Learning*, pages 19200–19227. PMLR, 2023.

354 [37] R. Linsker. Self-organization in a perceptual network. *Computer*, 21(3):105–117, 1988.

355 [38] I. Loshchilov and F. Hutter. Decoupled weight decay regularization. In *International Conference*
 356 *on Learning Representations*, 2019.

357 [39] Z. Ma and M. Collins. Noise contrastive estimation and negative sampling for conditional
 358 models: Consistency and statistical efficiency. In E. Riloff, D. Chiang, J. Hockenmaier,
 359 and J. Tsujii, editors, *Proceedings of the 2018 Conference on Empirical Methods in Natural
 360 Language Processing*, pages 3698–3707, Brussels, Belgium, Oct.-Nov. 2018. Association for
 361 Computational Linguistics.

362 [40] L. McInnes, J. Healy, and J. Melville. Umap: Uniform manifold approximation and projection
 363 for dimension reduction. *arXiv preprint arXiv:1802.03426*, 2018.

364 [41] M. Mohri, A. Rostamizadeh, and A. Talwalkar. *Foundations of Machine Learning*. Adaptive
 365 Computation and Machine Learning. MIT Press, Cambridge, MA, 2012.

366 [42] Y. Netzer, T. Wang, A. Coates, A. Bissacco, B. Wu, A. Y. Ng, et al. Reading digits in
 367 natural images with unsupervised feature learning. In *NIPS workshop on deep learning and
 368 unsupervised feature learning*, volume 2011, page 4. Granada, 2011.

369 [43] A. v. d. Oord, Y. Li, and O. Vinyals. Representation learning with contrastive predictive coding.
 370 *arXiv preprint arXiv:1807.03748*, 2018.

371 [44] J. Park, J. Lee, I.-J. Kim, and K. Sohn. Probabilistic representations for video contrastive learning.
 372 In *Proceedings of the IEEE/CVF conference on computer vision and pattern recognition*,
 373 pages 14711–14721, 2022.

374 [45] L. Perez and J. Wang. The effectiveness of data augmentation in image classification using deep
 375 learning. *arXiv preprint arXiv:1712.04621*, 2017.

376 [46] J. C. Peterson, R. M. Battleday, T. L. Griffiths, and O. Russakovsky. Human uncertainty
 377 makes classification more robust. In *Proceedings of the IEEE/CVF international conference on
 378 computer vision*, pages 9617–9626, 2019.

379 [47] Y. Polyanskiy and Y. Wu. *Information theory: From coding to learning*. Cambridge university
 380 press, 2025.

381 [48] B. Poole, S. Ozair, A. Van Den Oord, A. Alemi, and G. Tucker. On variational bounds of mutual
 382 information. In *International conference on machine learning*, pages 5171–5180. PMLR, 2019.

383 [49] A. Radford, J. W. Kim, C. Hallacy, A. Ramesh, G. Goh, S. Agarwal, G. Sastry, A. Askell,
 384 P. Mishkin, J. Clark, et al. Learning transferable visual models from natural language supervision.
 385 In *International conference on machine learning*, pages 8748–8763. PMLR, 2021.

386 [50] B. Rhodes and M. U. Gutmann. Variational noise-contrastive estimation. In *The 22nd Interna-
 387 tional Conference on Artificial Intelligence and Statistics*, pages 2741–2750. PMLR,
 388 2019.

389 [51] N. Saunshi, O. Plevrakis, S. Arora, M. Khodak, and H. Khandeparkar. A theoretical analysis
 390 of contrastive unsupervised representation learning. In *International Conference on Machine
 391 Learning*, pages 5628–5637. PMLR, 2019.

392 [52] C. Shorten and T. M. Khoshgoftaar. A survey on image data augmentation for deep learning.
 393 *Journal of Big Data*, 6(1):60, 2019.

394 [53] T. Song, J. Sun, X. Liu, and W. Peng. Scale-vae: Preventing posterior collapse in variational
 395 autoencoder. In *Proceedings of the 2024 Joint International Conference on Computational
 396 Linguistics, Language Resources and Evaluation (LREC-COLING 2024)*, pages 14347–14357,
 397 2024.

398 [54] Y. Tian, C. Sun, B. Poole, D. Krishnan, C. Schmid, and P. Isola. What makes for good views for
 399 contrastive learning? *Advances in neural information processing systems*, 33:6827–6839, 2020.

400 [55] M. Tschannen, J. Djolonga, P. K. Rubenstein, S. Gelly, and M. Lucic. On mutual information
 401 maximization for representation learning. *arXiv preprint arXiv:1907.13625*, 2019.

402 [56] M. Tschannen, J. Djolonga, P. K. Rubenstein, S. Gelly, and M. Lucic. On mutual infor-
 403 mation maximization for representation learning. In *International Conference on Learning
 404 Representations*, 2020.

405 [57] L. Van der Maaten and G. Hinton. Visualizing data using t-sne. *Journal of machine learning*
406 *research*, 9(11), 2008.

407 [58] W. I. Walker, H. Soulat, C. Yu, and M. Sahani. Unsupervised representation learning with
408 recognition-parametrised probabilistic models. In *International Conference on Artificial Intelli-*
409 *gence and Statistics*, pages 4209–4230. PMLR, 2023.

410 [59] B. Wang, Z. Tian, A. Ye, F. Wen, S. Du, and Y. Gao. Generative variational-contrastive learning
411 for self-supervised point cloud representation. *IEEE Transactions on Pattern Analysis and*
412 *Machine Intelligence*, 46(9):6154–6166, 2024.

413 [60] B. Wang, Z. Tian, A. Ye, F. Wen, S. Du, and Y. Gao. Generative variational-contrastive learning
414 for self-supervised point cloud representation. *IEEE Transactions on Pattern Analysis and*
415 *Machine Intelligence*, 2024.

416 [61] Q. Wang, S. R. Kulkarni, and S. Verdu. Divergence estimation for multidimensional densities
417 via k -nearest-neighbor distances. *IEEE Transactions on Information Theory*, 55(5):2392–2405,
418 2009.

419 [62] T. Wang and P. Isola. Understanding contrastive representation learning through alignment
420 and uniformity on the hypersphere. In *International conference on machine learning*, pages
421 9929–9939. PMLR, 2020.

422 [63] X. Wang, R. Zhang, C. Shen, T. Kong, and L. Li. Dense contrastive learning for self-supervised
423 visual pre-training. In *Proceedings of the IEEE/CVF conference on computer vision and pattern*
424 *recognition*, pages 3024–3033, 2021.

425 [64] D. Ward, M. Beaumont, and M. Fasiolo. SoftCVI: Contrastive variational inference with self-
426 generated soft labels. In *The Thirteenth International Conference on Learning Representations*,
427 2025.

428 [65] S. Xie and J. H. Giraldo. Variational graph contrastive learning. *arXiv preprint*
429 *arXiv:2411.07150*, 2024.

430 [66] J. Zbontar, L. Jing, I. Misra, Y. LeCun, and S. Deny. Barlow twins: Self-supervised learning via
431 redundancy reduction. In *International conference on machine learning*, pages 12310–12320.
432 PMLR, 2021.

433 [67] R. S. Zimmermann, Y. Sharma, S. Schneider, M. Bethge, and W. Brendel. Contrastive learning
434 inverts the data generating process. In *International conference on machine learning*, pages
435 12979–12990. PMLR, 2021.

436 **A Related work**

437 **A.1 Contrastive learning**

438 Self-supervised contrastive learning methods [8, 54] train an encoder $f: \mathcal{X} \rightarrow \mathcal{S}^{d_z-1}$ by drawing
439 semantically related views (positives) together in the embedding space while pushing unrelated views
440 (negatives) apart. In the standard setup, each example is treated as its own category, and only its
441 augmented copies count as positives. A variety of contrastive objectives—such as InfoNCE [43],
442 Debiased Contrastive Loss [10], Unbiased Contrastive Loss [2], triplet-based losses [9, 21], and
443 others—have been used to learn robust representations for tasks ranging from dense prediction in
444 computer vision [63] to multimodal alignment [49, 14, 28]. InfoNCE [43] in particular has been
445 shown to lower-bound mutual information [48], and subsequent work has revealed that its empirical
446 success hinges on a balance of *alignment* and *uniformity* in the learned embeddings [55, 62]. In the
447 supervised setting, SupCon [30] extends this idea by using class labels to define positive pairs among
448 same-class samples, often surpassing cross-entropy training in downstream performance. ProjNCE, a
449 generalization of SupCon [27], modifies SupCon loss so that it becomes a proper mutual information
450 lower bound.

451 **A.2 Probabilistic contrastive learning**

452 A growing body of work has begun to integrate probabilistic latent-variable modeling with contrastive
453 objectives. In the video domain, Park et al. represent each video clip as a Gaussian and combine them
454 into a mixture model, learning these distributions via a stochastic contrastive loss that captures clip-
455 level uncertainty and obviates complex augmentation schemes [44]. For 3D point clouds, Wang et al.
456 propose a Generative Variational-Contrastive framework that models latent features as Gaussians,
457 enforces distributional consistency across positive pairs by combining the variational autoencoder
458 and contrastive learning [60]. In graph representation learning, Xie and Giraldo introduce Subgraph
459 Gaussian Embedding Contrast, which maps subgraphs into a structured Gaussian space and employs
460 optimal-transport distances for robust contrastive objectives, yielding improved classification and
461 link-prediction performance [65].

462 On the theoretical front, Zimmermann et al. prove that contrastive objectives invert the data-generating
463 process under mild conditions, uncovering a deep connection to nonlinear independent component
464 analysis [67]. With a more generalized setting, Kirchhof et al. extend the InfoNCE loss so that the
465 encoder predicts a full posterior distribution rather than a point, and prove that these distributions
466 asymptotically recover the true aleatoric uncertainty of the data-generating process [32].

467 **A.3 Variational Inference and Contrastive Learning**

468 The most closely related line of work frames contrastive learning within a latent-variable inference
469 paradigm via Recognition-Parametrised Models (RPMs) [1, 58]. Aitchison and Ganev introduce
470 RPMs as a class of Bayesian models whose (unnormalized) likelihood is defined implicitly through
471 a recognition network [1]. They show that, under RPMs, the ELBO decomposes into mutual
472 information minus a KL term (up to a constant), and that for a suitable choice of prior the infinite-
473 sample InfoNCE objective coincides with this ELBO. Walker et al. consider RPMs by assuming
474 conditional independence of observations given latent variables, and develop an EM algorithm that
475 achieves exact maximum-likelihood learning for discrete latents along with principled posterior
476 inference [58].

477 Other works recast variational inference itself as a contrastive estimation task. Rhodes and Gutmann’s
478 Variational Noise-Contrastive Estimation (VNCE) derives a variational lower bound to the standard
479 NCE objective, enabling joint learning of model parameters and latent posteriors in unnormalized
480 models [50]. More recently, Ward et al. propose SoftCVI, which treats VI as a classification problem:
481 they generate “soft” pseudo-labels from the unnormalized posterior and optimize a contrastive-style
482 objective that yields zero-variance gradients at the optimum [64].

483 **A.4 Dimensional collapse**

484 In contrastive self-supervised learning, several approaches have been proposed to prevent dimen-
485 sional collapse by regularizing either the embedding projector or the second-order statistics of the

486 representations. Jing *et al.* [29] first demonstrated that, despite the repulsive effect of negative
 487 samples, embeddings can still collapse to a low-dimensional subspace due to a combination of strong
 488 augmentations and implicit low-rank bias in weight updates. They introduced DirectCLR, which fixes
 489 a low-rank diagonal projector during training; this projector enforces the embeddings to occupy a
 490 predetermined subspace and was shown empirically to outperform SimCLR’s learned linear projector.

491 Following this, several works have designed novel loss functions that explicitly regularize the
 492 covariance or cross-correlation of the embedding vectors. Ermolov *et al.* [12] apply a whitening MSE
 493 loss so that positive pairs match under mean-square error while enforcing identity covariance. Barlow
 494 Twins [66] minimize the deviation of the normalized cross-correlation matrix from the identity,
 495 effectively performing “soft whitening” to reduce redundancy. VICReg [3] further augments this
 496 idea by combining variance, invariance, and covariance regularizers to avoid collapse without using
 497 negative samples; notably, VICReg allows its two branches to use different architectures or even
 498 modalities, enabling joint embedding across data types. More recently, He *et al.* [17] showed that
 499 orthogonal regularization of encoder weight matrices preserves representation diversity and prevents
 500 collapse.

501 B Proofs

502 B.1 Proof of Lemma 3.1

503 *Proof.* With any auxiliary probability function $r(\mathbf{z}'|\mathbf{x})$ and Jensen’s inequality, we have

$$\begin{aligned} \mathbb{E}_{q(\mathbf{z}|\mathbf{x})}[\log p(\mathbf{x}|\mathbf{z})] &\geq \mathbb{E}_{q(\mathbf{z}|\mathbf{x})r(\mathbf{z}'|\mathbf{x})} \left[\log \frac{p(\mathbf{z}'|\mathbf{x})p(\mathbf{x}|\mathbf{z}')}{r(\mathbf{z}'|\mathbf{x})} \right] \\ &\stackrel{(a)}{=} \mathbb{E}_{q(\mathbf{z}|\mathbf{x})r(\mathbf{z}'|\mathbf{x})}[\log p(\mathbf{z}'|\mathbf{z})] + \mathbb{E}_{r(\mathbf{z}'|\mathbf{x})}[\log p(\mathbf{x}|\mathbf{z}')] + H(r(\mathbf{z}'|\mathbf{x})) \\ &= \mathbb{E}_{q(\mathbf{z}|\mathbf{x})q(\mathbf{z}'|\mathbf{x})}[\log p(\mathbf{z}'|\mathbf{z})] + \text{const.}, \end{aligned} \quad (21)$$

504 where (a) follows by choosing $r(\mathbf{z}'|\mathbf{x}) = q(\mathbf{z}'|\mathbf{x})$. This proves Lemma 3.1. \square

505 B.2 Proof of Proposition 3.2

506 *Proof.* Optimal critic [39] for InfoNCE satisfies that

$$\psi^*(\mathbf{x}, \mathbf{z}) \propto \log \frac{p(\mathbf{x}|\mathbf{z})}{p(\mathbf{x})} + \alpha(\mathbf{z}), \quad (22)$$

507 where $\alpha(\mathbf{z})$ only depends on \mathbf{z} . With the optimal critic, we then have

$$\begin{aligned} I_{\text{NCE}}(\mathbf{x}; \mathbf{x}') &= -\mathbb{E} \left[\log \frac{e^{\psi(\mathbf{z}, \mathbf{z}'_i)}}{\sum_{j=1}^N e^{\psi(\mathbf{z}, \mathbf{z}'_j)}} \right] \\ &= -\mathbb{E} \left[\log \frac{p(\mathbf{z}|\mathbf{z}'_i)}{\sum_{j=1}^N p(\mathbf{z}|\mathbf{z}'_j)} \right] \\ &= -\mathbb{E} \left[\log \frac{p(\mathbf{z}|\mathbf{z}'_i)}{\frac{1}{N} \sum_{j=1}^N p(\mathbf{z}|\mathbf{z}'_j)} \right] + \log N. \end{aligned} \quad (23)$$

508 Given \mathbf{z} , since $p(\mathbf{z}|\mathbf{z}'_j)$, $j \in \{1, 2, \dots, N\}$ are i.i.d. with $\mathbb{E}[p(\mathbf{z}|\mathbf{z}'_j)] = p(\mathbf{z}) < \infty$, the strong law
 509 of large numbers yields

$$\lim_{N \rightarrow \infty} \frac{1}{N} \sum_{j=1}^N p(\mathbf{z}|\mathbf{z}'_j) = p(\mathbf{z}). \quad (24)$$

510 The continuous mapping theorem then gives

$$\lim_{N \rightarrow \infty} \log \frac{p(\mathbf{z}|\mathbf{z}'_i)}{\frac{1}{N} \sum_{j=1}^N p(\mathbf{z}|\mathbf{z}'_j)} = \log \frac{p(\mathbf{z}|\mathbf{z}'_i)}{p(\mathbf{z})}. \quad (25)$$

511 Rearranging (22) and taking $N \rightarrow \infty$, we obtain

$$\begin{aligned} \lim_{N \rightarrow \infty} \{I_{\text{NCE}}(\mathbf{x}; \mathbf{x}') + \log N\} &= \lim_{N \rightarrow \infty} \mathbb{E} \left[\log \frac{p(\mathbf{z}|\mathbf{z}'_i)}{\frac{1}{N} \sum_{j=1}^N p(\mathbf{z}|\mathbf{z}'_j)} \right] \\ &\stackrel{(a)}{=} \mathbb{E} \left[\lim_{N \rightarrow \infty} \log \frac{p(\mathbf{z}|\mathbf{z}'_i)}{\frac{1}{N} \sum_{j=1}^N p(\mathbf{z}|\mathbf{z}'_j)} \right] \\ &= \mathbb{E} \left[\log \frac{p(\mathbf{z}|\mathbf{z}'_i)}{p(\mathbf{z})} \right], \end{aligned} \quad (26)$$

512 where the equality (a) follows by dominated convergence theorem that is verifiable using the fact that

$$\begin{aligned} \mathbb{E} \left[\log \frac{p(\mathbf{z}|\mathbf{z}'_i)}{\frac{1}{N} \sum_{j=1}^N p(\mathbf{z}|\mathbf{z}'_j)} \right] &= \mathbb{E} \left[\log p(\mathbf{z}|\mathbf{z}'_i) - \log \frac{1}{N} \sum_{j=1}^N p(\mathbf{z}|\mathbf{z}'_j) \right] \\ &\leq \mathbb{E} [\log g(\mathbf{z}) - \log \epsilon] \\ &\leq \log \mathbb{E} [g(\mathbf{z})] - \log \epsilon \\ &< \infty. \end{aligned} \quad (27)$$

513 Rewriting (26) gives

$$\begin{aligned} \lim_{N \rightarrow \infty} \{I_{\text{NCE}}(\mathbf{x}; \mathbf{x}') + \log N\} &= \mathbb{E} \left[\log \frac{p(\mathbf{z}|\mathbf{z}'_i)}{p(\mathbf{z})} \right] \\ &= \mathbb{E} \left[\log \frac{p(\mathbf{z}'_i|\mathbf{z})}{p(\mathbf{z}'_i)} \right] \\ &= \mathbb{E}_{q_\theta(\mathbf{z}'_i|\mathbf{x})q_\theta(\mathbf{z}|\mathbf{x})} [\log p(\mathbf{z}'_i|\mathbf{z})] + \mathbb{E}_{q_\theta(\mathbf{z}'_i|\mathbf{x})} [\log p(\mathbf{z}'_i)] \\ &= \mathbb{E}_{q_\theta(\mathbf{z}'_i|\mathbf{x})q_\theta(\mathbf{z}|\mathbf{x})} [\log p(\mathbf{z}'_i|\mathbf{z})] + \mathbb{E}_{q_\theta(\mathbf{z}'_i|\mathbf{x})} \left[\log \frac{p(\mathbf{z}'_i)}{q_\theta(\mathbf{z}'_i|\mathbf{x})} \right] + \mathbb{E}_{q_\theta(\mathbf{z}'_i|\mathbf{x})} [\log q_\theta(\mathbf{z}'_i|\mathbf{x})] \\ &= \mathbb{E}_{q_\theta(\mathbf{z}'_i|\mathbf{x})q_\theta(\mathbf{z}|\mathbf{x})} [\log p(\mathbf{z}'_i|\mathbf{z})] - D(q_\theta(\mathbf{z}'_i|\mathbf{x})\|p(\mathbf{z}'_i)) - H(q_\theta(\mathbf{z}'_i|\mathbf{x})). \end{aligned} \quad (28)$$

514 Substituting \mathbf{z}'_i into \mathbf{z}' , this concludes the proof of Proposition 3.2 \square

515 C Variational SupCon

516 C.1 Supervised Contrastive Learning

517 Khosla et al. [30] extend the InfoNCE loss from the self-supervised setting to a supervised context,
518 calling the resulting method *Supervised Contrastive Learning* (SupCon). When class labels $y_i \in$
519 $\{1, \dots, C\}$ are available, all samples sharing the same label can serve as positives.

Given a mini-batch $\{(\mathbf{x}_i, y_i)\}_{i=1}^B$, define for each anchor index a

$$\mathcal{A}(a) = \{1, 2, \dots, B\} \setminus \{a\}, \text{ and } \mathcal{P}(a) = \{p \in \mathcal{A}(a) : y_p = y_a\},$$

520 so that $\mathcal{P}(a)$ contains the indices of all positives for anchor a . The SupCon loss for anchor \mathbf{x}_a is then

$$I_{\text{SUP}}(\mathbf{x}_a) = -\frac{1}{|\mathcal{P}(a)|} \sum_{p \in \mathcal{P}(a)} \log \frac{\exp(s(\mathbf{z}_a, \mathbf{z}_p))}{\sum_{j \in \mathcal{A}(a)} \exp(s(\mathbf{z}_a, \mathbf{z}_j))}. \quad (29)$$

521 Averaging over all anchors in the batch yields the full objective:

$$\mathcal{L}^{\text{sup}} = \frac{1}{B} \sum_{a=1}^B I_{\text{SUP}}(\mathbf{x}_a). \quad (30)$$

522 **C.2 Variational SupCon (VSupCon)**

523 Building on the variational embedding pipeline of VSimCLR, VSupCon simply swaps the unsuper-
 524 vised InfoNCE term for the supervised contrastive loss while retaining the KL regularizer. Concretely,
 525 for each input \mathbf{x} with two augmentations $\mathbf{x}', \mathbf{x}''$, let the encoder output posterior parameters $(\boldsymbol{\mu}', K')$
 526 and $(\boldsymbol{\mu}'', K'')$, and sample normalized embeddings

$$\mathbf{z}' \sim \mathcal{P}\mathcal{N}(\boldsymbol{\mu}', K'), \quad \mathbf{z}'' \sim \mathcal{P}\mathcal{N}(\boldsymbol{\mu}'', K''). \quad (31)$$

527 Then the VSupCon objective is the symmetrized supervised loss plus the averaged, normalized KL:

$$\mathcal{L}^{\text{VSup}} = \frac{1}{2} \left(\mathcal{L}^{\text{sup}}(\mathbf{z}', \mathbf{z}'') + \mathcal{L}^{\text{sup}}(\mathbf{z}'', \mathbf{z}') \right) + \frac{1}{2d} \left(D(\boldsymbol{\mu}', K') + D(\boldsymbol{\mu}'', K'') \right). \quad (32)$$

528 Minimizing $\mathcal{L}^{\text{VSup}}$ therefore aligns same-class embeddings and regularizes their posterior distribu-
 529 tions toward the uniform prior on the sphere.

530 **D Discussion on the approximation in Section 3.1**

531 **D.1 Discussion on (8)**

532 The key step in our decoder-free ELBO maximization is the approximation

$$\mathbb{E}_{q_\theta(\mathbf{z}|\mathbf{x})} [\log p(\mathbf{x}|\mathbf{z})] \approx \mathbb{E}_{q_\theta(\mathbf{z}|\mathbf{x})q_\theta(\mathbf{z}'|\mathbf{x})} [\log p(\mathbf{z}'|\mathbf{z})] \quad (33)$$

533 **Lower-bound view.** As shown in Lemma 3.1, this approximation admits a lower bound up to an
 534 additive constant independent of \mathbf{z} :

$$\mathbb{E}_{q_\theta(\mathbf{z}|\mathbf{x})} [\log p(\mathbf{x}|\mathbf{z})] \geq \mathbb{E}_{q_\theta(\mathbf{z}|\mathbf{x})q_\theta(\mathbf{z}'|\mathbf{x})} [\log p(\mathbf{z}'|\mathbf{z})] + \text{const.} \quad (34)$$

535 Consequently, maximizing the right-hand side with respect to θ implicitly maximizes the reconstruc-
 536 tion term $\mathbb{E}_{q_\theta(\mathbf{z}|\mathbf{x})} [\log p(\mathbf{x}|\mathbf{z})]$, which is the objective of ELBO maximization. Moreover, using (10)
 537 (see Section 3.1), the surrogate is negatively related to InfoNCE:

$$\mathbb{E}_{q_\theta(\mathbf{z}|\mathbf{x})} [\log p(\mathbf{x}|\mathbf{z})] \approx -I_{\text{NCE}}(\mathbf{x}; \mathbf{x}'), \quad (35)$$

538 so minimizing the InfoNCE loss increases the reconstruction term.

539 **Change-of-variables view.** Another perspective on the reconstruction approximation (8) comes
 540 from a change of variables. Let g be an invertible, differentiable mapping such that $\mathbf{x} = g(\mathbf{z}')$. Then,
 541 by the change-of-variables formula,

$$p(\mathbf{x}|\mathbf{z}) = p(\mathbf{z}'|\mathbf{z}) |\det J_{g^{-1}}(\mathbf{x})| = p(\mathbf{z}'|\mathbf{z}) |\det J_g(\mathbf{z}')|^{-1}, \quad (36)$$

542 where J_g and $J_{g^{-1}}$ denote the Jacobians of g and g^{-1} , respectively, and $\mathbf{z}' = g^{-1}(\mathbf{x})$. Taking
 543 logarithms yields

$$\log p(\mathbf{x}|\mathbf{z}) = \log p(\mathbf{z}'|\mathbf{z}) + \log |\det J_{g^{-1}}(\mathbf{x})| = \log p(\mathbf{z}'|\mathbf{z}) - \log |\det J_g(\mathbf{z}')|, \quad (37)$$

544 where the second term depends only on \mathbf{x} (equivalently, on \mathbf{z}') and is independent of \mathbf{z} .

545 **Sufficient condition (tightness).** If, in addition to invertibility, g is *volume-preserving*, i.e.,
 546 $|\det J_{g^{-1}}(\mathbf{x})| \equiv 1$ (equivalently, $|\det J_g(\mathbf{z}')| \equiv 1$) on the data manifold, then the additive term
 547 in (37) vanishes and we obtain the tight equality $\log p(\mathbf{x}|\mathbf{z}) = \log p(\mathbf{z}'|\mathbf{z})$. More generally,
 548 when $|\det J_{g^{-1}}(\mathbf{x})|$ is approximately constant over the data manifold, the additive term acts as
 549 (approximately) a constant shift independent of \mathbf{z} , yielding a tight surrogate for optimization.

550 This assumption is plausible in practice under the commonly observed *dimension-collapse* phe-
 551 nomenon: the embeddings \mathbf{z}' have effective rank (intrinsic dimension) much smaller than the ambient
 552 embedding dimension yet retain nearly all task-relevant information about the features \mathbf{x} . When the
 553 feature and embedding manifolds have (approximately) the same intrinsic dimension and g behaves
 554 near-isometrically between them, the Jacobian determinant varies weakly, making the surrogate
 555 in (37) tight in practice.

Table 3: Gaussian KL (G-KL) vs. projected normal KL (PN-KL) on synthetic data.

	G-KL	PN-KL	Gap (G-KL–PN-KL)	Ratio (G-KL/PN-KL)
mean	106.86	97.37	9.49	0.91
std	9.56	7.63	-	-

556 D.2 Gaussian KL Surrogate for Projected-Normal KL

557 We study the tightness of the bound in (14), repeated here:

$$D(\mathcal{N}(\mu, K) \| \mathcal{N}(0, I_d)) \geq D(\mathcal{P}\mathcal{N}(\mu, K) \| \text{Unif}(\mathcal{S}^{d-1})). \quad (38)$$

558 Before analyzing tightness, we note several practical benefits of using the Gaussian KL as a surrogate
559 for the projected-normal KL:

- 560 • **Closed form.** It is trivial to implement and numerically stable.
- 561 • **Aligned optima.** The Gaussian KL and projected-normal KL share the same minimizer
562 (e.g., at $\mu = 0$ and $K = I_d$), so optimizing the surrogate steers the model toward the same
563 optimum.
- 564 • **Efficiency.** Unlike Monte Carlo or k -NN estimators needed for the projected-normal KL,
565 the Gaussian KL requires no sampling.

566 Moreover, the KL term acts only as a regularizer, whereas InfoNCE directly drives semantic similarity;
567 thus modest approximation error in the KL has limited effect on downstream performance.

568 We assess tightness by comparing the closed-form Gaussian KL with an estimated projected-normal
569 KL using a divergence estimator [61] in two settings: synthetic data and CIFAR-10 under VCL
570 training.

571 **KL gap on synthetic data.** We approximate $D(\mathcal{P}\mathcal{N}(\mu, K) \| \text{Unif}(\mathcal{S}^{d-1}))$ numerically using 10^5
572 samples in dimension $d = 128$ for random (μ, K) draws, with $\mu \sim \mathcal{N}(0, I_d)$ and

$$K = \frac{1}{d}AA^\top + 0.1I_d, \quad A_{ij} \sim \mathcal{N}(0, 0.5) \quad \forall i, j. \quad (39)$$

573 We employ the k -nearest-neighbor divergence estimator [61] with $k = 1$, compute both the Gaussian
574 KL (analytically) and the projected-normal KL (using the estimator) on the same samples, and repeat
575 over 20 random trials to reduce variance.

576 Table 3 reports the gap between the two KLS on synthetic data: the average absolute gap is approxi-
577 mately 9.49 (about a 10% relative difference). Thus, the Gaussian KL surrogate closely tracks the
578 projected-normal KL while retaining the practical advantages noted above.

579 **KL gap on CIFAR-10.** Beyond the synthetic study, we measure the gap during VCL training on
580 CIFAR-10 using the same experimental settings (Appendix E.1); results are shown in Figure 7. After
581 only a few epochs, the Gaussian KL and the projected-normal KL closely track each other. This
582 indicates that minimizing the Gaussian-KL surrogate effectively minimizes the projected-normal
583 KL—the quantity we aim to reduce—while retaining the practical advantages of the surrogate.

584 E Experiments

585 E.1 Training Details and Hyperparameters

586 **Datasets and preprocessing.** Experiments are conducted on CIFAR-10 [33], CIFAR-10C [19],
587 CIFAR-10H [46], CIFAR-100 [33], STL-10 [11], Tiny-ImageNet [35], and Caltech-256 [15]. We
588 train VCL models on CIFAR-10/100, Tiny-ImageNet, and Caltech-256, Tiny-ImageNet, and STL10.
589 Following SimCLR, we sample two views per image via random resized crop (image size 32×32 and
590 scale $[0.2, 1.0]$), horizontal flip ($p=0.5$), color jitter (brightness/contrast/saturation/hue = 0.4, applied
591 with $p=0.8$), Gaussian blur (kernel size 9), and random grayscale ($p=0.2$). Inputs are normalized
592 with dataset-specific means/standard deviations.

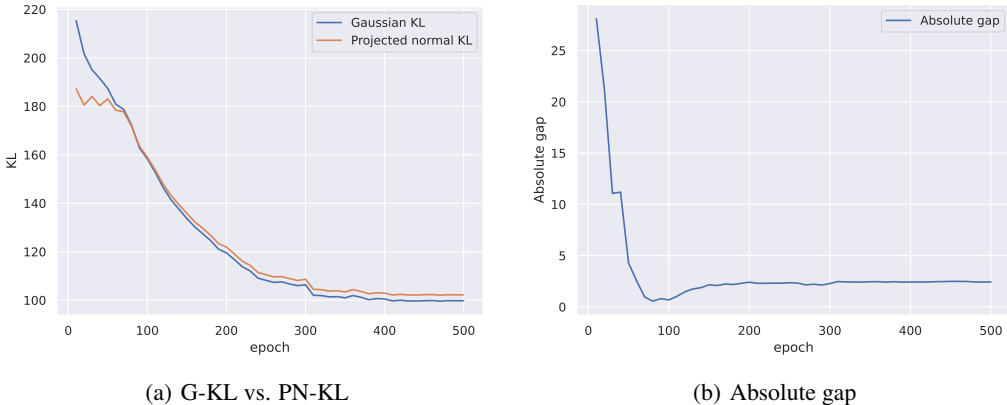


Figure 7: Tracking Gaussian KL (G-KL) and projected normal KL (PN-KL) during VCL training on CIFAR-10. (a) G-KL vs. PN-KL; (b) Absolute gap, $|G\text{-KL} - PN\text{-KL}|$. This shows that minimizing Gaussian KL leads to minimizing projected normal KL.

593 **Architectures.** We use ResNet-18 [18] as encoder and embedding dimension $d = 128$, and employ
 594 a linear classifier for downstream evaluations.

595 **Optimization.** We use AdamW [38] with base LR 10^{-2} (encoder and head), weight decay 10^{-4} ,
 596 batch size $B=512$, and $T=500$ epochs for pretraining and $T = 100$ for training linear classifier.
 597 Temperature for InfoNCE loss is $\tau=0.07$. We set $m=1$ posterior samples per view for VSimCLR
 598 and VSupCon by default (ablation in Table 5). No momentum encoder or queue is used; all negatives
 599 are in-batch. For training stability, we clip the posterior log-variance ($\log \sigma^2$) to $[-5, 5]$ to bound
 600 variances, and clip gradient global norm at 1.0.

601 E.2 Additional Results on Dimension Collapse

602 In addition to the singular spectrum of VCL embeddings on CIFAR-10 and CIFAR-100 in Figure 3,
 603 Figure 8 reports results on Caltech-256 and Tiny-ImageNet. In both datasets, VCL mitigates the
 604 dimension-collapse phenomenon commonly observed in contrastive learning.

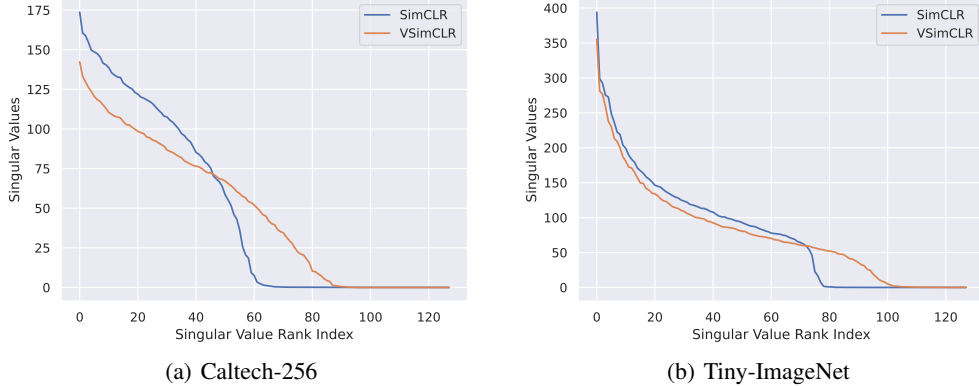


Figure 8: Singular-value spectrum of the embedding covariance on Cartech-256 and Tiny-ImageNet. VSimCLR mitigates dimensional collapse on both datasets.

605 E.3 Distributional Contrastive Loss

606 In addition to the contrastive loss on embeddings, it is worthwhile to contrast the posterior distributions
 607 within the VCL framework. Specifically, we aim to pull together the posteriors corresponding to

Table 4: Log-determinant of average posterior covariance K for each CIFAR-10 class.

Index	Class	$\log \det(K)$
0	airplane	-182.207
1	automobile	-181.691
2	bird	-183.713
3	cat	-191.317
4	deer	-184.969
5	dog	-185.432
6	frog	-182.125
7	horse	-179.331
8	ship	-185.991
9	truck	-188.179

Table 5: Classification accuracy on STL10 with different number of embedding generation from posterior. We report top-1 and top-5 accuracies of SimCLR, VSimCLR, SupCon, and VSupCon across the datasets with different m and DistNCE (40).

METHOD	STL10	
	TOP1	TOP5
SIMCLR	60.44	95.80
VSIMCLR ($m = 1$)	60.11	92.00
VSIMCLR ($m = 4$)	57.86	88.29
VSIMCLR ($m = 16$)	59.13	92.85
VSIMCLR ($m = 64$)	56.91	86.63
VSIMCLR WITH DISTNCE (40)	36.54	80.25
VSIMCLR (ASYM)	57.38	88.78
SUPCON	75.88	75.88
VSUPCON ($m = 1$)	75.76	96.99
VSUPCON ($m = 4$)	74.35	97.14
VSUPCON ($m = 16$)	76.11	98.39
VSUPCON ($m = 64$)	77.96	98.44

608 different augmentations of the same input and to push apart posteriors from distinct inputs. To
609 incorporate this into VCL, we introduce the *DistNCE* loss, a contrastive objective over posterior
610 parameters, defined as

$$D_{\text{DistNCE}}(\theta) = -\mathbb{E} \left[\log \frac{\exp(s(\theta, \theta^+))}{\sum_j \exp(s(\theta, \theta_j))} \right], \quad (40)$$

611 where θ denotes the posterior parameters (μ, K) , θ^+ is the positive-pair parameter for the same input,
612 and $\{\theta_j\}_{j \neq +}$ are negative-pair parameters from other inputs. The expectation is taken over the joint
613 distribution $p(\theta, \theta^+) \prod_{j \neq +} p(\theta_j)$.

614 Moreover, we increase the number of posterior samples used for the InfoNCE loss. Specifically, we
615 draw m samples $\{\mathbf{z}^{(k)}\}_{k=1}^m$ from each posterior, resulting in an m -fold increase in effective batch
616 size, and compute the InfoNCE loss over this enlarged set of embeddings. The classification results
617 are reported in Table 5.

618 We also evaluate the performance of the asymmetric lower bound (16) (denoted ASYM) in place of
619 the symmetrized objective (17). These results are also shown in Table 5.

620 From these experiments, we did not observe any significant differences when applying DistNCE (40),
621 using the asymmetric loss, or sampling multiple embeddings per posterior. Based on these findings,
622 we proceed with the basic VCL variants from the main text for all subsequent experiments.

Table 6: Classification accuracy on STL10 with different number of embedding generation from posterior. We report top-1 and top-5 accuracies of SimCLR, VSimCLR, SupCon, and VSupCon across the datasets with different m and DistNCE (40).

β	TOP-1 ACCURACY	TOP-5 ACCURACY
1	47.90	72.34
0.1	47.24	71.90
0.01	50.35	73.27
0.001	51.34	73.09



Figure 9: Sample images from the CIFAR-10, organized by class (columns) and sorted by their corresponding $\log \det(K)$ (rows). In each column, the top image has the highest $\log \det(K)$, the bottom image the lowest; the overlaid numbers indicate each image’s $\log \det(K)$.

623 E.4 Effect of KL Regularizer on Classification

624 As shown in Table 1, VSupCon exhibits reduced classification accuracy on some datasets, whereas
 625 VSimCLR remains stable. We attribute this degradation to two factors:

626 1. VSimCLR’s objective coincides with the VCL objective in (17), but VSupCon’s does not,
 627 creating a mismatch that can impede proper ELBO maximization.
 628 2. SupCon optimizes embeddings directly for classification; adding a KL term can conflict
 629 with this objective.

630 We therefore hypothesize that weakening the KL regularizer improves VSupCon’s accuracy. To test
 631 this, we scale the KL term by $\beta \in \{1, 10^{-1}, 10^{-2}, 10^{-3}\}$,

$$\mathcal{L}^{\text{vsup}}(\beta) = \mathcal{L}^{\text{sup}} + \beta D_{\text{KL}}(q_{\theta}(\mathbf{z} \mid \mathbf{x}) \parallel p(\mathbf{z})), \quad (41)$$

632 and evaluate the resulting embeddings. As expected, smaller β (i.e., a weaker KL effect) yields higher
 633 accuracy. Thus, for pure classification tasks, SupCon may not benefit from a VCL variant unless the
 634 KL weight is carefully tuned.

635 E.5 Implications of Distributional Embeddings

636 Distributional (probabilistic) embeddings provide useful capabilities, including uncertainty quantifi-
 637 cation and probability-based distances between samples and classes. We analyze them along three
 638 axes: uncertainty, typicality, and out-of-distribution (OOD) behavior.

639 **Posterior covariance vs. uncertainty.** As shown in Figure 9, different samples exhibit varying
 640 degrees of posterior dispersion (e.g., the log-determinant of the covariance, $\log \det(K)$), which can

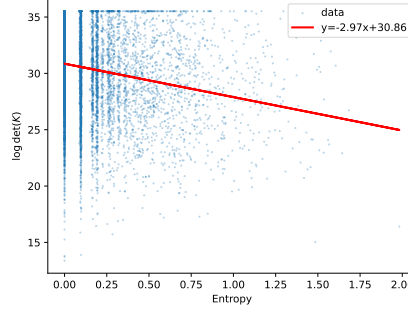


Figure 10: Relationship between posterior dispersion and label ambiguity. Each point plots the trace of K ($\text{tr}(K)$) against the entropy of human-annotated class probabilities from CIFAR-10H [46], with a first-order linear fit (red line). Similar to the result in Figure 5, the dispersion is negatively correlated with label ambiguity.

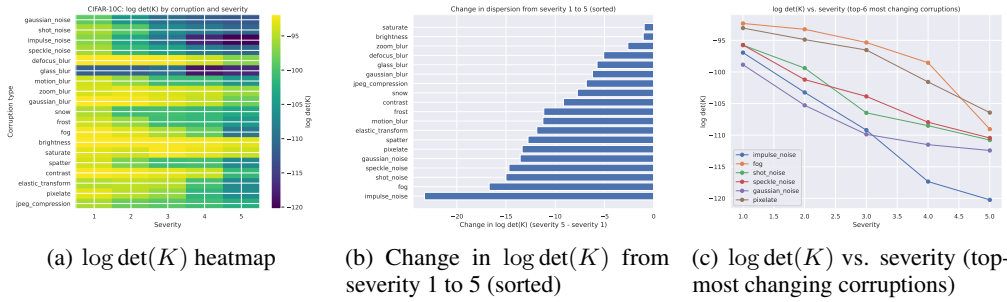


Figure 11: $\log \det(K)$ of **VSupCon** embeddings on CIFAR-10C [19] under different corruption types and severities. “Severity” denotes the corruption level. The observed negative correlation between $\log \det(K)$ and severity is consistent with our finding that more uncertain samples exhibit smaller posterior covariance dispersion. Exact $\log \det(K)$ values are in Table 8.

641 serve as an uncertainty measure. To examine how uncertainty and posterior covariance are related,
642 we conduct experiments on two benchmark datasets, CIFAR-10H [46] and CIFAR-10C [19]:

643 • **CIFAR-10H:** The test set provides soft labels [24, 25, 26] aggregated from multiple annotators.
644 Using these soft labels, we compute the per-sample label entropy as a measure of
645 uncertainty about the underlying class.

646 • **CIFAR-10C:** The test set provides systematically corrupted images with multiple corruption
647 types and severities (higher severity = stronger corruption), which induces greater label
648 ambiguity and thus higher uncertainty.

649 Beyond comparing $\log \det(K)$ with label entropy in Figure 5, we also compare the trace of K
650 (denoted $\text{tr}(K)$) against label entropy in Figure 10. In both cases, we observe a *negative* slope under
651 a first-order linear fit. This indicates that VSimCLR assigns **lower** posterior dispersion to inputs with
652 greater label uncertainty. Conversely, inputs that humans classify unambiguously—i.e., prototypical
653 class examples—exhibit posteriors with **larger** dispersion, suggesting their latent representations span
654 a broader region of the class-specific embedding space; ambiguous or outlier inputs yield **smaller**
655 dispersion, reflecting more concentrated latent distributions.

656 A similar pattern appears in Figures 6 and 11, which relate $\log \det(K)$ to corruption severity on
657 CIFAR-10C. We train VSimCLR and VSupCon on CIFAR-10 and evaluate their embeddings on
658 CIFAR-10C. Because higher severity entails stronger corruption and greater label ambiguity, these
659 figures further support the finding that posterior covariance dispersion is negatively correlated with
660 uncertainty. Tables 7 and 8 report the mean $\log \det(K)$ for each corruption type and severity level.

Table 7: Average $\log \det K$ of VSimCLR embeddings on CIFAR-10C for each corruption type and severity (higher severity = stronger corruption).

Corruption	Severity 1	Severity 2	Severity 3	Severity 4	Severity 5
gaussian_noise	-187.74	-189.85	-192.23	-193.05	-193.70
shot_noise	-187.49	-188.11	-190.18	-190.95	-191.97
impulse_noise	-188.25	-190.71	-192.61	-194.66	-194.82
speckle_noise	-187.59	-188.64	-189.21	-189.93	-190.48
defocus_blur	-184.41	-183.84	-182.67	-187.67	-186.76
glass_blur	-192.35	-191.76	-192.03	-194.36	-193.98
motion_blur	-185.83	-187.53	-189.88	-189.78	-191.94
zoom_blur	-185.95	-183.85	-183.86	-183.75	-185.07
gaussian_blur	-184.43	-182.83	-182.11	-183.47	-191.56
snow	-186.92	-189.86	-190.48	-193.08	-193.89
frost	-188.43	-190.13	-192.08	-192.16	-193.85
fog	-185.61	-187.61	-189.65	-193.37	-204.82
brightness	-184.89	-185.43	-186.17	-187.16	-189.70
saturate	-186.40	-191.14	-185.02	-186.36	-187.87
spatter	-186.32	-188.43	-191.12	-188.88	-191.03
contrast	-185.67	-188.03	-189.84	-192.59	-200.25
elastic_transform	-185.66	-185.12	-184.95	-189.66	-195.31
pixelate	-185.10	-186.44	-187.62	-188.58	-189.46
jpeg_compression	-182.94	-183.30	-183.73	-184.38	-185.28

Table 8: Average $\log \det K$ of VSupCon embeddings on CIFAR-10C for each corruption type and severity (higher severity = stronger corruption).

Corruption	Severity 1	Severity 2	Severity 3	Severity 4	Severity 5
gaussian_noise	-98.85	-105.28	-109.87	-111.50	-112.42
shot_noise	-95.76	-99.39	-106.47	-108.50	-110.77
impulse_noise	-96.94	-103.24	-109.20	-117.34	-120.23
speckle_noise	-95.73	-101.21	-103.87	-107.95	-110.44
defocus_blur	-91.95	-91.90	-92.33	-93.94	-97.03
glass_blur	-111.32	-111.29	-109.63	-118.74	-117.08
motion_blur	-93.95	-96.48	-100.86	-100.96	-105.21
zoom_blur	-93.66	-92.94	-93.67	-94.06	-96.29
gaussian_blur	-91.95	-92.31	-93.14	-94.40	-98.17
snow	-95.28	-100.62	-100.32	-101.30	-103.04
frost	-93.98	-96.23	-100.71	-101.33	-105.15
fog	-92.33	-93.25	-95.34	-98.54	-109.05
brightness	-92.04	-92.06	-92.16	-92.40	-93.11
saturate	-93.05	-93.80	-92.14	-92.82	-94.02
spatter	-93.86	-97.46	-100.59	-100.27	-106.63
contrast	-92.14	-92.54	-93.10	-94.30	-101.31
elastic_transform	-95.01	-94.65	-94.96	-100.26	-106.89
pixelate	-93.06	-94.88	-96.53	-101.58	-106.43
jpeg_compression	-95.47	-98.31	-99.28	-100.59	-102.32

661 This counterintuitive observation—that typical (i.e., common) samples exhibit larger posterior dispersion—parallels the concurrent findings of Guth et al. [16], albeit under different settings: (i)
662 **Quantity:** we analyze latent-space posterior dispersion via $\log \det K$, whereas they study input-space
663 marginal density $p(x)$; (ii) **Observation:** typical samples have larger $\log \det K$ (ours), while they
664 have lower $p(x)$ (theirs). Although these quantities live in different spaces, both results indicate that
665 typical samples are not the highest-density points. In our case, typical images yield larger dispersion
666 and atypical images smaller dispersion; since dispersion is inversely related to peak density, our result
667 is consistent with Guth et al. Hence, in both settings, “typical” \neq “highest-density.” Consequently,
668

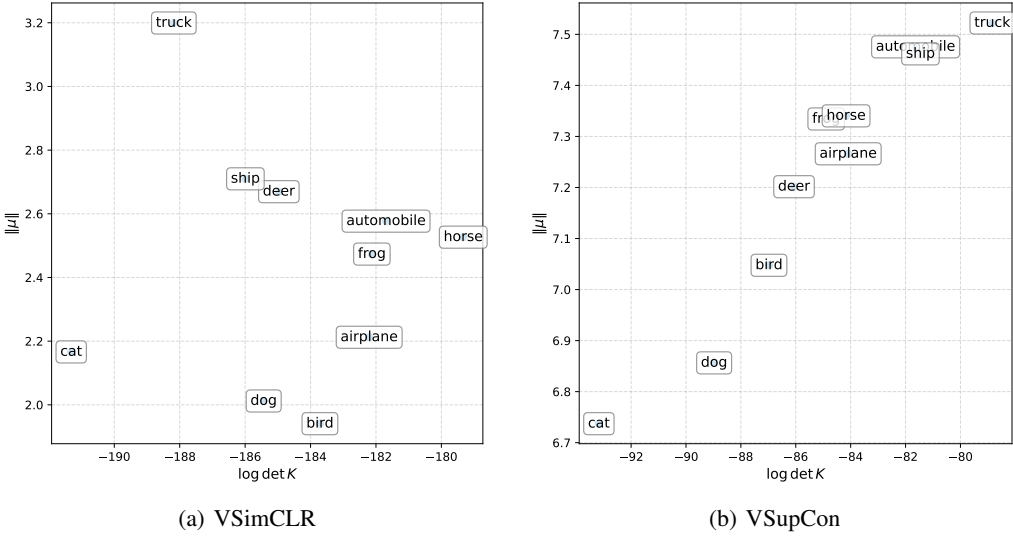


Figure 12: Norm of the posterior mean $\|\mu\|$ versus the log-determinant of the covariance $\log \det(K)$, averaged per class. Both μ and K are computed by averaging over all samples belonging to the same class.

669 posterior dispersion serves as a useful uncertainty signal; see Table 2 for an application under label
670 scarcity.

671 **Class-wise average posterior parameters.** Figure 12 reports class-wise averages of the posterior
672 parameters—the mean norm $\|\mu\|$ and the covariance dispersion $\log \det K$ —for VSimCLR and
673 VSupCon. Classes exhibit distinct dispersion profiles. Despite being trained independently, the two
674 methods yield similar class-wise patterns in both quantities: for example, the *cat* and *dog* classes
675 show comparatively lower $\|\mu\|$ and $\log \det K$, whereas *truck* attains the largest $\|\mu\|$. Table 4 provides
676 detailed per-class $\log \det K$ values.

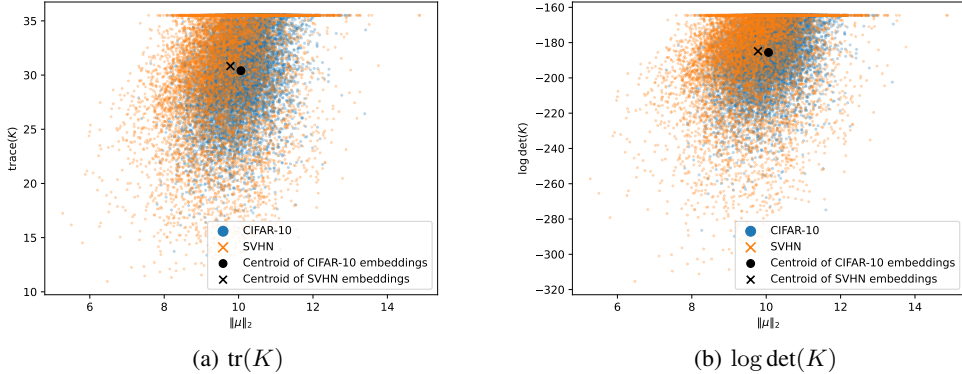


Figure 13: Posterior parameters of CIFAR-10 and SVHN datasets. We use the same encoder of VSimCLR trained with CIFAR-10.

677 **Posterior on in-distribution vs. out-of-distribution.** We compare per-sample posterior parameters
678 under VSimCLR for in-distribution (ID; CIFAR-10) versus out-of-distribution (OOD; SVHN [42])
679 inputs. VSimCLR is trained on the CIFAR-10 training set, after which we extract (μ, K) on the
680 CIFAR-10 and SVHN test sets. Figure 13 plots the pairs $(\|\mu\|, \log \det K)$ for each dataset; black
681 markers denote dataset-wise means. While the mean values $\text{avg}(\|\mu\|)$ and $\text{avg}(\log \det K)$ are similar

682 across CIFAR-10 and SVHN, the SVHN points exhibit substantially greater spread (dispersion)
683 across samples, indicating a broader posterior-parameter distribution for OOD data.